Boundary-Layer Meteorology (2005) 117: 37–71
DOI 10.1007/s10546-004-1130-3

VERTICAL HEAT TRANSFER IN THE LOWER ATMOSPHERE OVER THE ARCTIC OCEAN DURING CLEAR-SKY PERIODS

JEFFREY D. MIROCHA*, BRANKO KOSOVIĆ[1] and JUDITH A. CURRY[2]
Program in Atmospheric and Oceanic Sciences, University of Colorado, Boulder, CO 80309-0311, U.S.A.; [1]*Lawrence Livermore National Laboratory, Livermore, CA 94550-9234, U.S.A.;* [2]*School of Earth and Atmospheric Sciences, Georgia Institute of Technology, Atlanta, GA 30332-0340, U.S.A.*

(Received in final form 16 April 2004)

Abstract. A diagnostic study of heat transfer within the lower atmosphere and between the atmosphere and the surface of the Arctic Ocean snow/ice pack during clear-sky conditions is conducted using data from the Surface Heat Budget of the Arctic Ocean (SHEBA) field experiment. Surface heat budgets computed for four cloudy and four clear periods show that, while the net turbulent heat fluxes at the surface are small during the cloudy periods, during the clear-sky periods they are a considerable source of surface heating, balancing significant portions of the conductive heat fluxes from within the snow/ice pack. Analysis of the dynamics and thermodynamics of the lower atmosphere during the clear-sky periods reveals that a considerable portion of the heat lost to the surface by turbulent heat fluxes is balanced by locally strong heating near the atmospheric boundary-layer (ABL) top due to the interaction of subsiding motions with the strong overlying temperature inversions surmounting the ABL. This heat is then entrained into the ABL and transported to the surface by turbulent mixing, maintained by a combination of vertical wind shear and wave-turbulence interactions. The frequency of stable, clear-sky periods, particularly during the winter, combined with these results, suggests that the downward transfer of heat through the lower atmosphere and into the surface represents an important component of the heat budgets of the lower atmosphere and snow/ice pack over the annual cycle.

Keywords: Stable atmospheric boundary layer, Surface heat budget, Turbulent heat flux.

1. Introduction

The Arctic has been identified as a region of great importance to global climate due in part to the many powerful feedback mechanisms occurring both within the Arctic and between the Arctic and the lower latitudes (e.g., IPCC, 2001; Przybylak, 2003). The atmospheric boundary layer (ABL) is of relevance to many of these feedback processes, as many of the complex interactions between surface and cloud optical and thermal properties are mediated by ABL processes (Curry et al., 1996).

The ubiquity of clouds is a hallmark of the Arctic atmosphere. Several cloud climatologies conducted in the Arctic region indicate that cloud

* E-mail: mirocha@colorado.edu

occurrence peaks as high as 80–90% during the summer, falling to a minimum of 40–68% during winter, with low clouds dominating the variability over the annual cycle (e.g., Huschke, 1969; Hahn et al., 1984; Warren et al., 1988). When clear-sky ice crystal precipitation is included, the winter minimum is estimated to increase to 80% (Curry et al., 1996). During the yearlong Surface Heat Budget of the Arctic Ocean (SHEBA) field experiment of 1997–1998, clouds were observed to occur over the Arctic Ocean interior on average 85% of the time. During the least cloudy season (winter), the average occurrence of clouds diminished to 73%, with a minimum of 63% during the month of February (Intrieri et al., 2002a).

Although by any accounting the Arctic must be considered 'cloudy', even during the peak cloudy season, clear-sky conditions are observed 10–20% of the time. During the winter, the fraction of cloud-free days increases to 32–60%. The winter during the SHEBA experiment featured clear-sky conditions 27% of the time, with many stretches of several consecutive cloud-free days, and longer periods of predominantly clear-sky conditions, punctuated only occasionally by brief episodes of cloudiness. As these percentages reflect cloud of variable height and thickness appearing anywhere within the field of view, these percentages underpredict functionally clear conditions with respect to surface and lower atmosphere energy exchange processes.

The energy exchange processes occurring at the surface change markedly depending on the presence or absence of clouds. During the low-sun seasons, such changes are magnified by the weak-to-nonexistent solar radiation, as well as the extreme cold and dry conditions of the arctic atmosphere. Analysis of four predominantly clear-sky periods during the SHEBA experiment indicates a substantial turbulent transfer of heat from the atmosphere to the surface during each period. The loss of heat from the lower atmosphere due to these fluxes implies strong cooling of the shallow region of the atmosphere in turbulent contact with the surface. However, no such lower-atmospheric cooling is observed during these periods.

This apparent dilemma raises the question of the source of atmospheric heating required to offset the cooling of this layer due to the loss of heat to the surface. Motivation for the search for this mechanism involves the considerable portions of both the lower-atmospheric and surface heat budgets represented by sensible heat fluxes exchanged at the snow/ice-atmosphere interface during these periods, especially during the clear winter periods, and by extension, similar periods occurring throughout the year. A necessary condition for the maintenance of these large sustained heat fluxes without simultaneous cooling of the lower atmosphere is heating of comparable magnitude within the portion of the atmosphere in turbulent contact with the surface.

The implications for the snow/ice pack are potentially significant. During the three clear winter periods, the average sensible heat flux at the surface

balanced a significant portion of the estimated conductive heat flux, implying a reduction of the cooling rates within the snow/ice pack from those implied by the average net radiative fluxes alone. If the balance of terms in the surface heat budget is similar during the 20–60% of the annual cycle during which such conditions proliferate, then this heat transfer process may be of considerable relevance to the snow/ice pack as well.

Given the importance of this flow of energy within the lower atmosphere to the lower atmosphere and surface energy budgets, a careful analysis of the various components of the heat transfer processes occurring within the lower atmosphere during stable, clear-sky conditions is needed.

Section 2 describes the data used in this study. Section 3 discusses the roles of the various surface fluxes on the surface heat budgets and how they change between cloudy and clear-sky conditions. Section 4 discusses the thermodynamic processes occurring within the lower atmosphere during clear-sky periods. Section 5 discusses the nature of lower-atmospheric turbulence and its role in the vertical transport of heat during clear-sky periods. Section 6 summarizes the results of the study.

2. Data

Most of the data utilized herein were obtained during the SHEBA field experiment. As described more thoroughly elsewhere (e.g., Uttal et al., 2002), the SHEBA experiment consisted of an extensive suite of instrument sites coordinated about a Canadian Coast Guard icebreaker (the *Des Groseilliers*) frozen into the Arctic Ocean pack ice. The entire field camp drifted with the pack ice for a full year, covering approximately 1400 km along the trajectory depicted in Figure 1, providing a time series of atmospheric and surface data corresponding to the vertical column centered about the field camp, over one annual cycle.

The data relevant to the present study were obtained from three *in situ* measurement platforms, the Atmospheric Surface Flux Group (ASFG) site, the GPS/Loran Atmospheric Sounding System (GLASS), and the National Center for Atmospheric Research (NCAR) C-130 research aircraft.

2.1. ASFG TOWER

The ASFG site utilized a 20-m tower outfitted with a variety of meteorological sensors as well as several measurement devices on the surface surrounding the tower to measure many surface and lower-atmospheric fields. The parameters of interest to this study and the measuring instruments used by the ASFG are given in Table I.

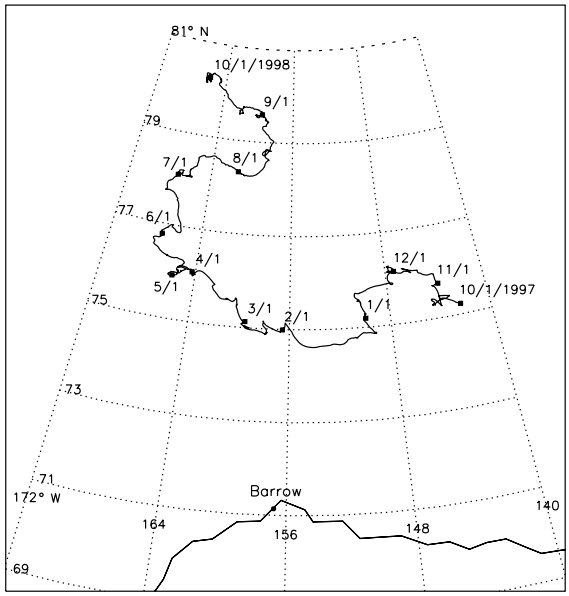

Figure 1. Trajectory of the SHEBA field camp.

TABLE I

Summary of instrumentation and parameters measured at ASFG tower site, from Persson et al. (2002).

Instrument	Measured parameters
Väisälä T/RH probe	Temperature, relative humidity
Applied Technologies Inc. sonic anemometers	Three-dimensional velocity
Ophir fast hygrometer	Specific humidity
Eppley pyrgeometers	Longwave radiation
Eppley pyranometers	Shortwave radiation
General Eastern thermometer, Barnes PRT-5	Surface temperature
Väisälä PTB 220B digital barometer	Surface pressure
Thermistors	Snow and ice temperature

Many redundant measurements were obtained from the instrument suite given in Table I, allowing for evaluation, correction, and error estimation for most of the measured parameters. Estimated errors for the key variables used in this study are given in Table II.

Hourly averaged spectra and cospectra were obtained from 10 Hz measurements at nominally five heights on the tower (only one height for specific humidity). The velocity data were aligned in the streamwise direction, given

TABLE II
Estimated errors for selected parameters in the ASFG dataset, from Persson et al. (2002).

Parameter	Random error (hourly)
Temperature	±0.05 K
Surface temperature	±0.6 K
Net shortwave radiation	±4.5%
Net longwave radiation	±4 W m^{-2}
Latent heat flux	±50%
Sensible heat flux	
Hourly	±3 W m^{-2}
Daily average	±1.8 W m^{-2}
Monthly average	±0.3 W m^{-2}
Conductive flux	> ±100%

by the average velocity during the longest period of unbroken data occurring during the given hour. The data were then parsed into data blocks of 13.65-min duration (corresponding to 2^{13} data points), which were linearly detrended and Hamming-windowed. The hourly averaged spectra and cospectra were obtained by averaging over the nominally seven overlapping data blocks obtained from each hour of data. The $\overline{w'u'}$, $\overline{w'q'}$ and $\overline{w'T'_{sn}}$ covariances, where w', u' , q' and T'_{sn} are the perturbation vertical velocity, streamwise velocity, specific humidity and sonic virtual temperature, respectively, were then obtained from integration across the [0.2 s, 13.65 min] frequency interval. The hourly averaged friction velocity, u_*, and sensible and latent heat fluxes, F_{SH} and F_{LH}, respectively, were then computed from

$$u_* = -(\overline{w'u'})^{1/2}, \tag{1}$$

$$F_{\mathrm{SH}} = \rho C_p \overline{w'T'} = \rho C_p(\overline{w'T'}_{sn} - 0.51\overline{w'q'}), \tag{2}$$

$$F_{\mathrm{LH}} = \rho(L_{\mathrm{e}} + L_{\mathrm{f}})\overline{w'q'}. \tag{3}$$

Here C_p is the heat capacity at constant pressure, ρ is the density and L_{e} and L_{f} are the latent heats of evaporation and fusion, respectively. During times when the covariance $\overline{w'q'}$ was unavailable, bulk estimates were obtained using a modified version of the coupled ocean atmosphere response experiment (COARE) sea-air flux algorithm, the details of which may be found in Fairall et al. (1996). Due to the higher data recovery of the bulk $\overline{w'q'}$, these values were used in (2) to compute the sensible heat fluxes.

Some of the spectra shown in this report reveal the presence of noise at the higher frequencies. As the focus of this study is chiefly concerned with the lower-frequency portions of the spectra, these errors at high frequencies are

not considered to be crucially important to any of the significant conclusions of this study.

Further details of the instrumentation and data processing used in the creation of the ASFG dataset may be found in Persson et al. (2002), or at the SHEBA ASFG website (http://www.weather.nps.navy.mil/~psguest/sheba/).

2.2. Soundings

Vertical profiles of atmospheric temperature, relative humidity and wind speed above the ASFG tower were obtained from Väisälä RS 80-15GH radiosondes, launched from the ship deck approximately every 12 h, at roughly 1100 and 2300 UTC, throughout the year. From April through July, the twice daily soundings were augmented by two additional soundings per day, occurring at approximately 0500 and 1700 UTC.

Missing data within the radiosonde ascents above approximately 50 m were replaced with linearly interpolated values. Errors occurring below approximately 50 m, during the first few moments of the launch, while the radiosonde was accelerating from rest and unspooling, were corrected by smoothly joining the highest available ASFG tower value to the lowest wind speed maximum. A quadratic function of height was chosen for the corrected wind speed profiles, as the behaviour of the quadratic function generally fit the endpoints of the interpolation domain better than linear or logarithmic functions. While this functional form may not be correct in some details, the shape of the wind speed profile below 50 m is not crucial to the results of this study. Scatter in the radiosonde temperature and relative humidity data very close to the surface was eliminated by using linearly interpolated values between the the highest ASFG tower and the height within the profile at which the scatter decreased to an acceptable level, generally significantly below 50 m. All missing ASFG data both in time and height were replaced by linearly interpolated values. All data above approximately 50 m were smoothed using seven-point running mean values.

2.3. Aircraft measurements

Several turbulence measurements in the lower atmosphere were conducted during the spring and summer from the NCAR C-130 research aircraft. High-frequency (25 Hz) temperature and velocity measurements were obtained using a Rosemount thermometer and gust probe, respectively.

The spectra and cospectra were computed by parsing the data stream into N intervals of 60-s each (corresponding to a distance of approximately 6–7 km). Only periods of straight, level flight were utilized. The segments

were subsequently detrended, then separated into mean and perturbation states. The spectra and cospectra were then obtained by averaging over the N data blocks. The variances and covariances were obtained from these averages by integration across the spectrum from a specified low-frequency endpoint.

The NCAR Research Aviation Facility filtered mechanical effects from the data, however some noise is evident at the high frequencies.

2.4. Anciliary measurements

Three additional data fields used in this study that were not obtained during the SHEBA experiment are the vertical velocity, temperature advection and radiative heating rates.

As routine atmospheric profiling was conducted at only one location, little spatial data were obtained above the surface, preventing estimation of vertical motion from the divergence, or calculation of advection. These quantities must therefore be obtained from other sources. One source of these terms is a large-scale atmospheric model in which these fields are predicted. The vertical velocities and advections were calculated for the SHEBA column in this manner using the European Centre for Medium Range Weather Forecast (ECMWF) model, initialized with SHEBA data. Unfortunately the coarse vertical resolution of these datasets near the surface undermines their applicability to the present study. The roles of vertical motion and advection in the context of the extremely shallow ABLs that are the focus of the present study are examined using bulk thermodynamic budgets applied to a stratified lower atmosphere over a nearly steady 72-h period, as described in Section 4.

Radiative heating rates were obtained for the same 72-h period using the rapid radiative transfer model (RRTM) (Mlawer et al., 1997) implemented into a single-column model (SCM). The radiative heating rates were computed at approximately 10 m resolution in the lower atmosphere by running the SCM with observed profiles of temperature and water vapour, a broadband surface albedo of 0.85, and surface emissivity = 0.99.

3. Surface Heat Budgets

In the absence of precipitation, the heat budget for a slab of ice representing the surface portion of the Arctic Ocean pack ice may be written

$$\frac{\partial T}{\partial t} = \frac{1}{\rho C_p \Delta z}[F_C - F_{SH} - F_{LH} - F_{RAD}]. \tag{4}$$

In (4) T is the layer mean temperature, t is the time, ρ is the layer mean density, C_p is the layer mean heat capacity at constant pressure, F_C is the

conductive heat flux from below, F_{SH} is the sensible heat flux, F_{LH} is the latent heat flux, F_{RAD} is the net radiative flux, Δz is the layer thickness and positive values correspond with an upward flow of energy.

Time series of variables relevant to the surface heat budgets during the four predominantly cloudy and four predominantly clear-sky periods are given in Figures 2 and 3, respectively. The upper portions of each panel show time series of latent and sensible heat fluxes, and net (longwave + shortwave) radiative flux at the surface. In each figure, three periods are taken from the

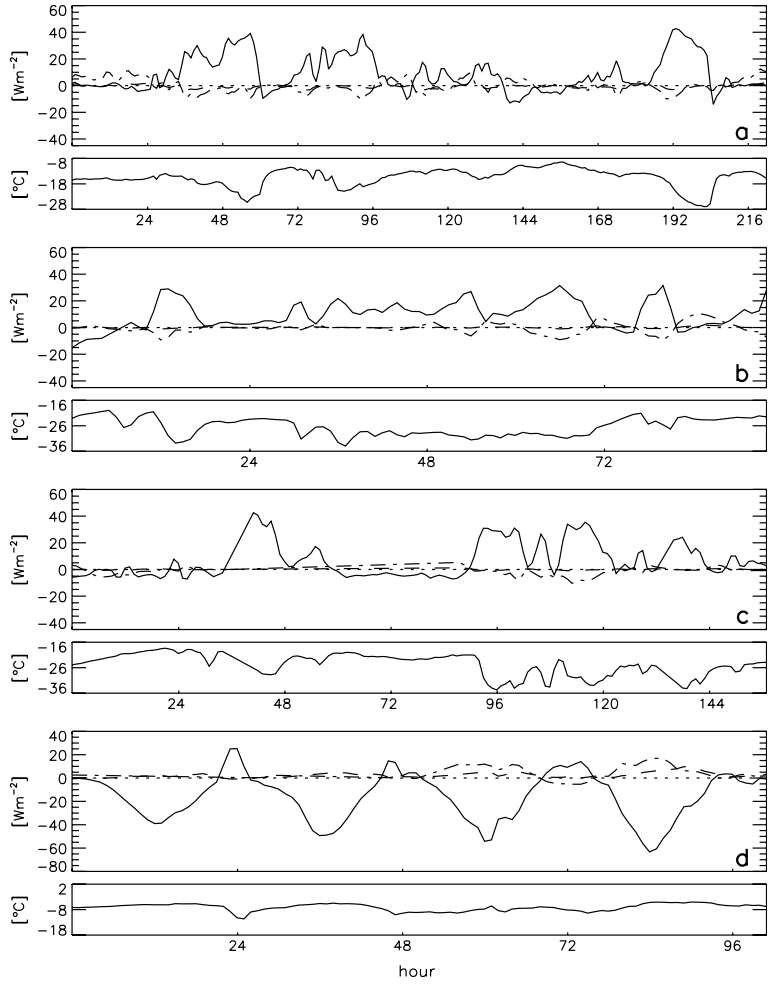

Figure 2. Surface energy budget terms measured at SHEBA during four predominantly cloudy periods. Panel a: 11/5/1800–11/15/0000; panel b: 1/7/0800–1/11/0600; panel c: 2/26/0800–3/4/2100; panel d: 5/12/0900–5/16/1400. Dashed lines indicate latent heat fluxes, dot-dash lines indicate sensible heat fluxes, solid lines indicate net (longwave + shortwave) radiative fluxes, dotted lines indicate zero. Small panels below indicate surface temperature.

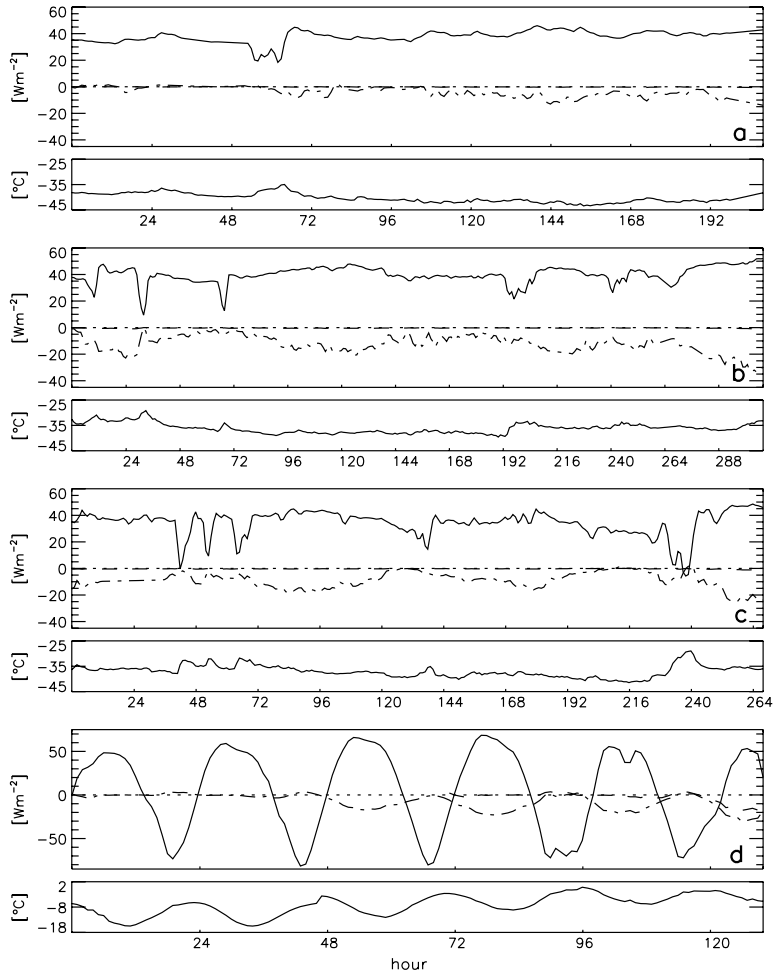

Figure 3. Surface energy budget terms measured at SHEBA during four predominantly clear-sky periods. Panel a: 12/24/0500–1/1/2100; panel b: 1/12/0300–1/24/2300; panel c: 2/09/1200–2/20/1600; panel d: 5/22/0200–5/27/1200. Dashed lines indicate latent heat fluxes, dot-dash lines indicate sensible heat fluxes, solid lines indicate net (longwave + shortwave) radiative fluxes, dotted lines indicate zero. Small panels below indicate surface temperature.

low-sun seasons, with one period taken from the high-sun season. The lower panels show a time series of surface temperature. The horizontal axis depicts the length of time in 24-h segments from the beginning of each period. All time and date identifiers throughout the paper, unless otherwise indicated, are given in the mm/dd/hhhh format, where mm is the number of the month, dd is the day of month, and hhhh is the hour and minute.

Contrasting the cloudy and clear periods demonstrates the impact of clouds on the physical processes influencing the surface heat budget. As

Figures 2 and 3 show, when clouds replace clear skies, downwelling longwave radiation increases significantly, causing the surface to warm. This warming of the surface relative to the air above induces a flux of sensible heat from the surface to the atmosphere, enhancing mixing in the lower portion of the ABL. When the downwelling radiative fluxes remain almost steady with time, the surface temperatures equilibrate to almost steady values as well. The large downwelling radiative fluxes prevent large surface-to-air temperature gradients from forming, and the turbulent heat fluxes at the surface remain small.

When skies clear, the downwelling longwave radiative fluxes incident upon the surface diminish substantially due to the extreme cold and dry conditions typical of the arctic atmosphere replacing the warmer, highly emissive cloud. The small downwelling radiative fluxes occurring throughout most of the year (except during portions of the high-sun season), combined with the high surface emissivity and albedo, result in strong radiative cooling of the surface. The interaction between strong radiative cooling of the surface and turbulent mixing in the lower atmosphere results in a considerable flux of sensible heat from the atmosphere into the surface. During quiescent conditions, the radiative cooling, turbulent heat fluxes and surface temperatures reach almost steady values, with the radiative cooling exceeding the turbulent heat fluxes by a considerable amount.

These findings mirror several assessments of the influence of polar clouds on the surface. Curry and Ebert (1992), Schweiger and Key (1994), Zhang et al. (1996), and Walsh and Chapman (1998) all have shown that the net effect of polar clouds is to warm the surface during all but short durations of the high-sun season. Intrieri et al. (2002b) and Persson et al. (2002) confirmed these results during the SHEBA experiment. Their analyses of the annual cycle of surface turbulent heat fluxes during the SHEBA experiment likewise confirmed that, in general, surface turbulent heat fluxes acted to warm the surface during clear periods, but were small during cloudy periods.

During each of the periods discussed above, the net change in surface temperature was less than 1 K. Hence, an approximate balance may be assumed between processes heating and cooling the surface. As all of the physical processes occurring above the surface have been accounted for, any energy imbalance among those processes implies a compensating flux of heat toward the surface from below. In this manner, an average conductive flux reaching the surface may be estimated as the residuum among the sum of the time-averaged surface fluxes.

The data in Table III summarize the general results presented above. Average values of the net radiative, latent and sensible heat fluxes at the surface observed during each of the periods discussed above are given along with two estimates of the average conductive flux reaching the surface. The first estimates are the residuals among the average measured surface fluxes,

TABLE III
Average surface fluxes (W m^{-2}) for four cloudy and four clear periods.

Period	Sky	Net Longwave	Net Shortwave	Latent	Sensible	Conductive	C
11/5/1800–11/15/0000	Cloudy	8.82	−0.003	−0.61	0.12	8.33 ± 5.68	7.55
1/7/0800–1/11/0600	Cloudy	9.92	0	0.07	−0.52	9.47 ± 5.68	7.44
2/26/0800–3/4/2100	Cloudy	8.25	−1.16	0.16	−0.17	7.08 ± 5.64	5.59
5/12/0900–5/16/1400	Cloudy	11.90	−28.08	2.39	3.37	−10.41 ± 8.09	0.62
12/24/0500–1/1/2100	Clear	37.78	0	−0.15	−3.9	33.72 ± 5.48	14.10
1/12/0300–1/24/2300	Clear	39.80	0	−0.36	−12.35	27.09 ± 5.36	12.74
2/09/1200–2/20/1600	Clear	34.79	−0.63	−0.31	−8.99	24.86 ± 5.45	10.50
5/22/0200–5/27/1200	Clear	57.39	−51.76	2.62	−7.40	0.85 ± 9.21	0.97

Positive values indicate upward fluxes, ± values indicate errors in conductive flux estimates given by data in Table II. C are conductive fluxes computed by Persson et al. (2002), with error > ± 100%.

with the range of values given by the error estimates in Table II. The last column presents the average conductive fluxes computed by Persson et al. (2002) using

$$C = -k_s[(T_s - T_{ice})/d_s]. \tag{5}$$

Here k_s is the thermal conductivity coefficient, T_s is the surface (radiative) temperature, T_{ice} is the temperature at the ice/snow interface, and d_s is the snowpack depth. The temperatures used in (5) were obtained from thermistor probes buried in the snowpack near the ASFG tower, and a value of 0.3 was used for the thermal conductivity coefficient.

As Table III shows, during some of periods, the residuals among the average surface fluxes were much larger than the fluxes computed by Persson et al. (2002). The reasons for these discrepancies are potentially many. One source of disagreement is that their calculations pertain to the bulk flux across the depth of the snowpack, whereas ours reflect the flux just below the surface. As such, their calculations ignore the effects of nonlinearity of the temperature profile within the snow layer near the surface. Another source of uncertainty is the value of k_s (e.g., Maykut, 1982). Although a value of $k_s = 0.3$ was used in (5), the measured value of 0.14 was approximately a factor of two smaller (Sturm et al., 2001). The larger value, similar to those measured during previous conductivity studies, was used in (5), due to inconsistencies between the measured value and the observed accretion of ice at the ice/ocean interface during the winter season (Sturm et al., 2004).

4. The Lower Atmosphere

Contours of temperature and time-height sections of wind speed in the lowest 750 m of the atmosphere during the four clear-sky periods discussed in the previous section are presented in Figure 4. Temperature is shown in this figure to distinguish the strong, narrow temperature inversion surmounting the shallow ABL occurring during each of these periods. Comparison with Figure 3 shows a strong relationship between wind speed and sensible heat flux at the surface; however the relationship between wind speed and ABL height appears weaker.

4.1. Atmospheric boundary layer

As seen in Figure 4, during the four predominantly clear-sky periods the highly variable lower atmospheric temperature stratification revealed a broad

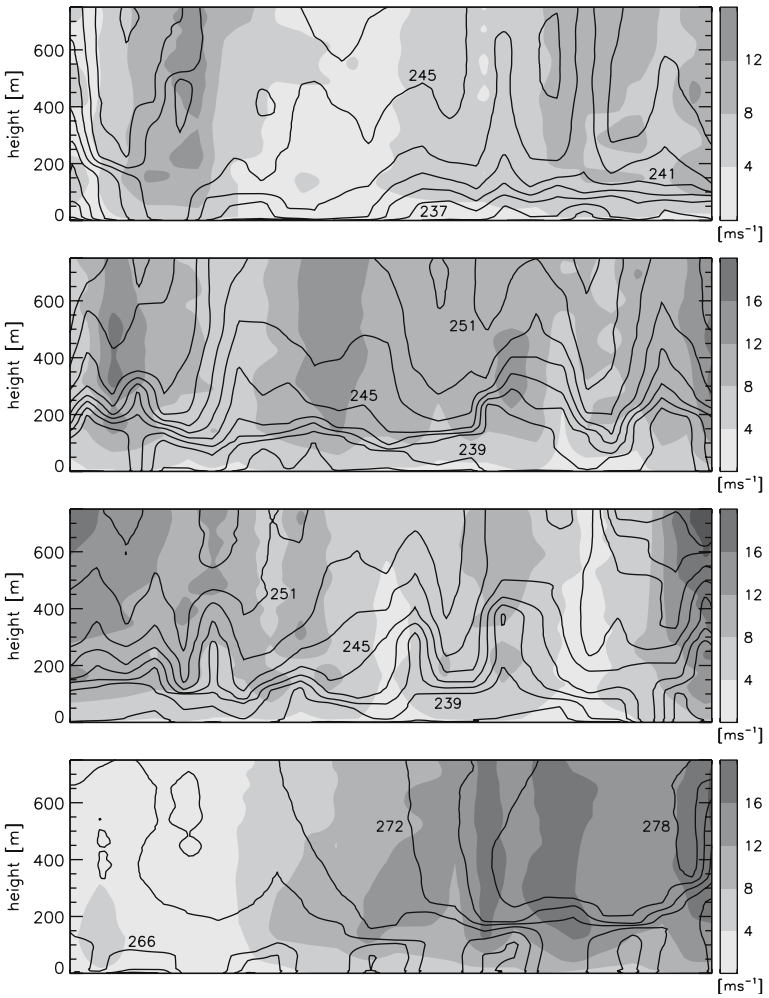

Figure 4. Contours of temperature and time-height sections of wind speed in the lowest 750 m of the atmosphere measured at SHEBA during four clear-sky periods. Panel a: 12/24/0500–1/1/2100; panel b: 1/12/0300-1/24/2300; panel c: 2/09/1200–2/20/1600; panel d: 5/22/0200–5/27/1200.

range of ABL structures. During these periods, the lower atmosphere generally yielded a four-layer structure, featuring a strongly stratified surface layer below a more strongly mixed boundary layer, surmounted by a strong overlying temperature inversion, with a layer of weaker stratification above. Brief portions of these periods featured episodes of very strong stability, due to weak winds and strong surface cooling, during which little discernible ABL structure is evident from the temperature profiles. However, most of the periods exhibited continuous turbulence of weak-to-moderate intensity due

to the presence of vertical wind shear and the reservoir of heat beneath the surface.

The spring period was influenced by a significant diurnal solar cycle. During the first 36 h of the spring period surface-based convection gave rise to strong mixing during the afternoons, followed by very stable conditions overnight due to the weak winds and strong surface cooling. During the latter stages of the spring period, increasing winds maintained elevated shear-driven mixing overnight, while acting to stabilize the ABL during the daytime by enhancing entrainment of warm air into the ABL top. Throughout these periods, the observed ABLs were as close to being horizontally homogeneous as one can expect to find in the nature, with no evidence of density currents or flows generated by horizontal temperature gradients, for instance.

Classification of ABL structure and estimation of its height during the stable portions of these periods can be difficult under any circumstances, but is especially so in the absence of measurements suitable to making such distinctions. Few direct measurements of turbulence were made above the ASFG tower, none during the low-sun seasons. Aircraft flights conducted during May indicate contributions to velocity and temperature variability from a wide range of length scales within a weakly stable ABL, with a pronounced shift to larger length scales in the more stable layer above. Spectra computed from the ASFG tower suggest a general decrease in turbulence intensity and a migration of spectral power toward larger length-scale processes with increasing static stability. Additionally, many of the hourly averaged surface and ASFG tower variables show increasing hour-to-hour variability with increasing stability.

Transitions between the following idealized ABL structures could explain these observations. Periods featuring weakly stable temperature profiles and moderate wind speeds likely reflect predominantly shear-driven mixing near the surface, with global intermittency occurring in the more stable environment near the ABL top (Kim and Mahrt, 1992), due in part to locally large wind shear values near the low-level jet (Smedman, 1988), wave activity (Forrer and Rotach, 1997), or a combination of the two. Such a structure would fit within the *traditional boundary-layer* classification, in which turbulence is primarily forced by surface roughness (Mahrt and Vickers, 2001). During periods of increasing stability, turbulence within the ABL likely becomes less strongly connected to, and less continuous near, the surface due to a proportional decrease in shear-driven mixing near the surface relative to turbulence generation aloft via above mentioned processes. With yet further increases in stability the turbulence field within the ABL becomes dominated by turbulence generation aloft, resulting in an *upside down* ABL structure. In such cases, while turbulence remains primarily detached from the surface, intermittent bursts of turbulence occasionally penetrate through the ABL, reaching the surface (Mahrt, 1999).

Mason and Derbyshire (1990) showed that the large-eddy simulation (LES) technique was a useful tool for studying the stably stratified ABL. Using LES model simulations of the stably stratified ABL, Andrén (1995), Kosović and Curry (2000) and Saiki et al. (2000) have demonstrated the existence of a two-layer structure, with shear-driven turbulence near the surface, surmounted by a layer dominated by wave activity. Andrén (1995) also documented global intermittency occurring within the ABL, with increasing intermittency near the ABL top. The intermittency resulted in turbulent bursting events, which significantly enhanced vertical fluxes.

The absence of discriminatory measurements also hinders the estimation of ABL height. One commonly employed discriminator of the ABL top is the height at which the turbulent shear stress decreases to a small fraction of its surface value (e.g., Zilitinkevich and Mironov, 1996). Similar arguments using the vertical heat flux have been employed (e.g., Derbyshire, 1990). Obviously, for non-traditional ABLs that are not strongly connected to the surface, the use of surface stresses is not applicable. A third commonly employed diagnostic technique for locating the top of the ABL is an increase in the gradient Richardson number

$$Ri = \frac{g}{S^2\theta}\frac{\partial\theta}{\partial z}, \tag{6}$$

beyond a critical value, Ri_c (e.g., Handorf et al., 2000). Here, $S = |\partial U/\partial z|$, where U is the scalar wind speed, and $\theta = T(1000/p)^{R/Cp}$ is the potential temperature, with p in hPa, and R is the gas constant for dry air. While values of $Ri_c = 0.2-0.25$ are frequently cited in the literature (e.g., Handorf et al., 2000), within stable ABLs significant turbulent mixing has been observed at Ri values well in excess of these critical values (e.g., Larsen et al., 1990; Sempreviva et al., 1992). As argued in Kosović and Curry (2000), use of a vanishing turbulent stress is the most appropriate discriminator of the stable ABL top, as it definitively distinguishes turbulent and non-turbulent layers, while allowing for a significant vertical flux of heat that may occur via wave activity occurring near the stable ABL top. Within the very stable ABL, as turbulent shear stresses may intermittently cease, the vanishing would have to be taken in a time-averaged sense.

Due to the absence of direct turbulence measurements and uncertainties in the wind speed profiles, and in light of the above discussion, in this study *ABL* will refer to the layer of the atmosphere extending from the surface to the base of the overlying temperature inversion, as this height coincides with an abrupt decrease in turbulent shear stresses, readily discernible from the temperature profiles. When referring to periods of several days' duration, ABL should be interpreted in a time-averaged sense.

4.2. Heat budgets

During each of the four clear-sky periods discussed herein, a considerable flux of heat was transferred from the ABL to the surface. An estimate of the bulk cooling ΔT (in K) of a layer of depth Δz due to a flux of sensible heat extracted from it may be calculated from

$$\Delta T = \frac{\int_{t_0}^{t} F_{\mathrm{SH}}\, d\tau}{\rho C_p\, \Delta z}, \tag{7}$$

where t_0 is the initial time, and each of the remaining terms has been identified previously. It is noted that bulk properties refer to layers that are well mixed, which the atmosphere above the surface clearly is not. However, in the context of the analysis to follow, the use of bulk arguments applies.

Table IV presents the estimated net cooling and cooling rates of the lowest 100 m of the atmospheric column, taken to represent the ABL, using a representative density of $1.5\,\mathrm{kg\,m^{-3}}$. The range of errors in the bulk cooling estimates reflect the errors in the sensible heat fluxes, calculated from the data given in Table II. In spite of the significant losses of heat given in Table IV, examination of Figure 4 shows no such cooling during these periods. As such, other physical processes occurring within the layer of the atmosphere in turbulent contact with the surface must have been contributing significant amounts of heat during each period.

Assuming that radiative and turbulent fluxes vary mainly in the vertical, and ignoring viscous dissipation, the time rate of change of temperature for a clear-sky atmosphere may be written

$$\frac{\partial T}{\partial t} = -u\frac{\partial T}{\partial x} - v\frac{\partial T}{\partial y} - w\frac{\partial T}{\partial z} - w\frac{g}{C_p} - \frac{1}{\rho C_p}\frac{\partial F_{\mathrm{RAD}}}{\partial z} - \frac{1}{\rho C_p}\frac{\partial F_{\mathrm{T}}}{\partial z}. \tag{8}$$

In (8) u and v are the zonal and meridional velocity components, respectively, x and y are the zonal and meridional directions, respectively, w is the vertical velocity, z is the height, g is the acceleration due to gravity, F_{T} is the turbulent heat flux, and all other terms have been identified previously.

TABLE IV

Estimated bulk cooling and cooling rates of the 100 m deep column above the surface during four clear-sky periods.

Period	Bulk cooling (K)	Cooling rate ($\mathrm{K\,day^{-1}}$)
12/24/05–1/1/21	19.49 ± 7.00	2.24 ± 0.80
1/12/03–1/24/23	91.17 ± 8.75	7.08 ± 0.68
2/09/12–2/20/16	57.75 ± 8.17	5.15 ± 0.73
5/22/02–5/27/12	23.15 ± 4.91	4.24 ± 0.90

A discussion of the roles of each of the physical processes in (8) within the context of the large-scale synoptic conditions and surrounding physical environment during the four extended clear-sky periods is given next. A detailed examination of the nearly steady 72-h period, 1100 15 January to 1100 18 January, provides the framework for estimates of the unknown terms in (8). During this period the lower atmosphere is idealized as three layers, the lower of which representing the ABL, the 100-m deep layer above the ABL representing the overlying temperature inversion layer, and the 200-m deep layer above the inversion layer representing the free atmosphere. While the two lower layers are assumed to be in turbulent contact with each other and with the surface, the free atmosphere is assumed to be decoupled.

4.3. Surface turbulent heat flux

During the nearly steady period the average ABL depth was approximately 93 m. The bulk cooling of a layer of this depth due to an average sensible heat loss of $12.80 \pm 1.70\,\mathrm{W\,m^{-2}}$ is $23.67 \pm 3.14\,\mathrm{K}$.

4.4. Radiation

The estimated bulk radiative heating within the ABL during the nearly steady period was 1.89 K. The estimated bulk radiative cooling of the inversion and free atmosphere layers were approximately 2.25 and 4.15 K, respectively, during the same time.

Reliable error estimates for the radiative heating can not be obtained due to uncertainties in numerous radiatively important parameters, most importantly the presence of ice crystals and aerosols in the atmosphere. During one predominantly cloud-free test period of 72-h duration, the RRTM predicted a mean downwelling longwave radiative flux at the surface of $124.23\,\mathrm{W\,m^{-2}}$ with a range of $10.69\,\mathrm{W\,m^{-2}}$, whereas the ASFG measured a mean of $150.05\,\mathrm{W\,m^{-2}}$ with a range of $60.6\,\mathrm{W\,m^{-2}}$. The higher mean and considerably greater range of the measured fluxes suggests the inability to model the above mentioned factors accurately. Although it is not possible to infer an error in atmospheric heating rates from these calculations, they do suggest that the error is likely to be small enough so that the modelled values can be taken as representative.

From the time-height sections given in Figure 4 it can be seen that when clouds are present the ABL warms considerably. However it appears that during predominantly cloud-free periods featuring brief episodes of cloudiness, radiation does not play a significant role in offsetting the strong ABL cooling. Even more so than during clear skies, the net effect of low, non-

precipitating clouds on the temperature of the lower atmosphere as a whole is a cooling one, as the cloud tops radiate strongly in the cold, dry arctic atmosphere.

4.5. Horizontal temperature advection

During the nearly steady period, the observed bulk warming of the inversion and free atmosphere layers were approximately 2.89 and 2.25 K, respectively, small fractions of the nearly 27 K estimated bulk ABL cooling due to the surface fluxes. Therefore, for horizontal temperature advection to have supplied the heat to balance the ABL cooling, either a strong cooling mechanism must have existed above the ABL to counteract the strong advective heating assumed to have been occurring there as well, or the advective heating profile must have attenuated rapidly from large magnitudes within the ABL to much smaller values above.

Potential cooling mechanisms above the ABL are radiation and vertical temperature advection, as the temperature structure above the ABL precludes any upward fluxes of heat. During each of the clear-sky periods discussed in this report, the temperature above the ABL increased with height. Hence, if vertical motions were responsible for cooling the air above the ABL, the air must have been rising. Sustained rising motions during anticyclonic conditions, nearly perpetual clear skies and sustained high surface pressures are unlikely, leaving radiative cooling as the only physical process capable of counteracting advective heating above the ABL.

The presence of low clouds would have augmented cooling above the ABL, however only small and temporally brief periods of cooling related to cloudiness can be inferred from Figure 4, suggesting that the cumulative effects of cloud-top cooling were small over the durations of these predminantly clear-sky periods.

From these considerations it follows that for horizontal advection to have contributed significant heating within the the ABL, its magnitude must have peaked sharply within the ABL and attenuated rapidly above. On physical grounds, such a profile shape is unlikely. A column of warm air advecting over a cold surface would be expected to cool most rapidly at its base, where turbulent exchanges with the cold surface could remove heat from it more quickly than any physical process occurring aloft, during clear skies. The profile of advective heating would therefore be expected to diminish in magnitude with increasing proximity to the surface on thermodynamic grounds. Dynamic considerations suggest that a warm air mass encountering a dome of cold air near the surface would rise buoyantly and flow over the colder layer. Based on these considerations, strong heating within the ABL by horizontal advection must be considered unlikely.

4.6. Turbulent heat flux

A turbulent flux of heat into the ABL from above could have provided the heat required to balance the cooling of the ABL to the surface. However, since turbulence can only transport heat from one region to another, a downward flux of heat into the ABL implies the removal of the same amount of heat from the layer above. As the atmosphere immediately above the ABL features strong static stability, turbulent mixing would be expected to diminish rapidly above the ABL. Hence, any heat transferred into the ABL must have come from a shallow layer immediately above it. However, the region immediately above the ABL experienced no observable strong cooling to offset the loss of heat to the layer below. A sustained deepening of the ABL could have supplied such heating through entrainment of the warm air above it, however no such sustained deepening was observed.

4.7. Vertical temperature advection

Vertical temperature advection must have supplied the heat to the ABL layer to balance its loss of energy to the surface. As vertical velocities are typically quite small, one would not immediately expect the vertical advection of temperature to be a likely candidate to have generated such strong heating. However, as advection is the product of both a velocity and the gradient of the advected quantity, in the presence of sufficiently strong temperature gradients, even small vertical velocities can generate locally large heating rates.

Table V shows the estimated bulk heating (in K) for three atmospheric layers during the nearly steady period, along with a summary of the remaining measured and computed terms in (8). The temperature budgets for the three layers are computed as follows. The cooling of the ABL due to sensible heat flux at the surface and the warming due to radiation are compared to the observed temperature change. The difference reflects the amount

TABLE V

Estimated total contributions (in K) to the heat budgets of the three lower atmospheric layers discussed in the text during the nearly steady period using subsidence rates of 1.427± 0.169 mm s^{-1}.

Layer	F_{SH}	F_{RAD}	Observed ΔT		$w[\frac{\partial T}{\partial z} + \frac{g}{C_p}]$	Residual
Free atmosphere	0	−4.15	2.25	6.40	8.05 ± 0.95	1.65 ± 0.95
Inversion	0	−2.25	2.89	5.14	26.54 ± 3.14	0
ABL	23.67 ± 3.14	1.89	−0.37	21.40 ± 3.14	0	0

of heating ΔT in K, required to balance the ABL heat budget. The heat budget of the inversion layer is computed from the radiative temperature change of that layer relative to the observed temperature change, yielding a ΔT required to close that layer's temperature budget. A vertical advection is then calculated that, when acting on the observed bulk temperature gradient of the inversion layer, closes the heat budgets of each of the two lower layers. It is assumed that the strong heating within the inversion layer is transferred into the ABL by vertical heat fluxes and entrainment, then through the ABL and into the surface. Heating due to vertical motion within the ABL is ignored in this approximation. A similar heat budget calculation is carried out for the free atmosphere, within which the effects of vertical motions interacting with that layer's bulk temperature gradient are incorporated. The residual from that layer then may be interpreted as an estimate of the large-scale horizontal temperature advection. Warming due to adiabatic compression is included with the vertical advection term in the upper two layers.

As seen from Table V, a very modest mean subsidence rate of $1.427\,\mathrm{mm\,s^{-1}}$ nearly closes the heat budgets of each of the three layers due to the large differences in their bulk temperature gradients. The average free atmosphere bulk temperature gradient of $0.012\,\mathrm{K\,m^{-1}}$ is only 19.36% of the average inversion layer bulk temperature gradient of $0.062\,\mathrm{K\,m^{-1}}$. Although a degree of uncertainty in the details of these estimates is acknowledged, the close agreement between the widely divergent heating rates of each of these three layers relative to to their assumed cooling profiles supports the arguments presented in this section. The extension of this model to the other predominantly clear-sky periods seems straightforward in light of their evolving thermodynamic structures relative to the thermodynamic processes occurring within the lower atmosphere. While strong heating within the lowest few hundreds of metres via radiation and horizontal temperature advections must be considered unlikely, very modest subsidence rates interacting with the strong temperature inversions occurring throughout these periods could easily have generated heating of sufficient magnitudes to have balanced the strong cooling of the ABL to the surface.

4.8. Synoptic considerations

The synoptic-scale weather patterns occurring during these periods reinforce the likelihood of non-trivial subsidence rates leading to significant vertical temperature advection while the horizontal temperature advection was small. During the nearly steady period, strong high pressure dominated the region, yielding predominantly north-westerly winds ranging from 4.7 to $11.2\,\mathrm{m\,s^{-1}}$ within the ABL, with a maximum velocity of $14.3\,\mathrm{m\,s^{-1}}$ in the free atmosphere layer above. The nearly cloud-free conditions over a large region

surrounding the SHEBA site suggest that a significant sustained difference in the aggregate surface temperature of the neighbouring upstream region was unlikely. The generally high surface pressures and anticyclonic synoptic-scale conditions occurring during each of the clear-sky periods reinforce the likelihood of significant subsidence rates while horizontal temperature advections were small.

The arrival of a storm at the conclusion of the spring period suggests that a significant portion of the atmospheric warming may have been due to horizontal temperature advection in the warm sector of the approaching storm. Although horizontal temperature advection may have been significant during the last few days of this late spring period, the likelihood of such strong, sustained horizontal advective heating decreases during the low-sun seasons, due to the cold surface and the seasonal migration of the mid-latitude storm track to the south. The near-surface thermal properties of an air mass advecting from such a distance would be strongly modified during the long transit.

The model that emerges from the above analysis for heat transfer in the lower atmosphere over the Arctic Ocean during clear-sky periods is that of heat extraction from the ABL by surface fluxes being predominantly balanced by entrainment of warm air into the ABL from above. The cooling of the region above the ABL in response to its loss of heat to the ABL below is, in turn, significantly balanced by strong local heating generated via the interaction of large-scale subsiding motions with the large temperature gradients occurring there.

While large-scale horizontal advection is certainly a net source of warming for the arctic atmosphere, during these stable, clear-sky periods any significant net heating due to horizontal temperature advection occurs at a considerable distance above the ABL, with the net heating of the lowest several hundreds of metres accomplished primarily by the effects of vertical motions.

It remains to identify the mechanisms for the entrainment of this heat into the ABL and for its diffusion down to and exchange with the surface. In the following section, high-frequency temperature and wind velocity data measured at the ASFG site and during two aircraft flights are analyzed to further investigate the vertical heat exchange processes occurring in the lower atmosphere during these periods.

5. Turbulent Heat Transfer

During clear-sky periods over the Arctic Ocean, turbulence is rarely initiated by surface heating, as the high emissivity and albedo of the ice pack conspire to maintain surface temperatures that are cooler than those of the atmosphere above most of the time. As such, surface turbulent heat fluxes are typically a sink for turbulence kinetic energy within the ABL. Instead, the

primary sources of turbulence kinetic energy are surface roughness, vertical wind shear and breaking waves.

The static stability of the lower atmosphere during each of the clear-sky periods discussed in this report provides a restoring force for any vertical displacements, and is therefore conducive to the generation of gravity waves. (e.g., Stull, 1988). Once triggered, gravity waves may amplify and eventually break, giving rise to mixing processes which augment turbulent fluxes occurring within the affected region (e.g., Nappo, 2002). Vertical shearing of the wind may also generate Kelvin–Helmholtz waves, both a direct source of turbulence, and a mechanism for gravity wave excitation (e.g., Hooke et al., 1973). Turbulence may be generated intermittently by the passage of a wave train or the cyclical generation of Kelvin–Helmholtz waves, resulting in a succession of such turbulent bursting episodes, although in the mean the ABL may appear stable (e.g., Kondo et al., 1978).

Atmospheric wave activity has been observed in stably stratified regions of the lower atmosphere in diverse environments spanning the globe (e.g., Nappo, 1990; Cheung, 1991). In the lower latitudes, they commonly occur during the night following the collapse of the convectively mixed ABL. In the high latitudes, they are observed to occur much more frequently as, in many respects, the high-latitude ABL simulates a perpetual nocturnal ABL during much of the year.

Of particular interest to the present study is the interaction between waves and turbulence. Chimonas (1980), Finnigan and Einaudi (1981), Fua et al. (1982) and Finnigan (1988) discuss in detail several mechanisms through which gravity waves and turbulence may interact with one another. Some of these mechanisms allow energy to flow back and forth between the wave and turbulence fields. Under certain circumstances, energy may be extracted from the mean flow by the wave-turbulence combination. Due to such energy exchange processes, waves and turbulence may persist for long periods of time in environments far removed from the forcing mechanisms typically associated with their genesis. In this section evidence is presented for the existence of waves and wave-turbulence interaction over the interior of the Arctic Ocean during two clear-sky periods.

5.1. Clear winter period

No aircraft measurements of turbulence were conducted during the winter. However, high-frequency temperature and wind velocity data were recorded at the ASFG site.

Figure 5 depicts spectra of vertical velocity and temperature from a height of approximately 14 m on the ASFG tower during two periods in mid-January, one near the middle of the nearly steady period discussed in the pre-

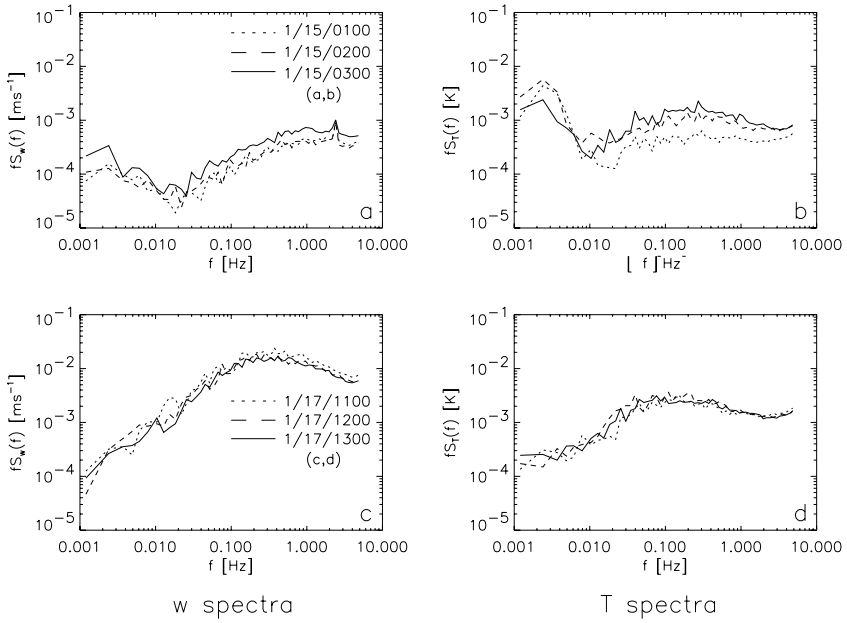

Figure 5. Vertical velocity spectra (panels a, c) and temperature spectra (panels b, d) obtained from the ASFG tower during mid-January.

vious section, and one few hours before it began. In this paper, all of the spectral powers are multiplied by their frequency, as indicated by the fS_η labels on the ordinate axes for spectra of variable η. Spectra from the three consecutive hours identified in the legend show the intensity and the range of physical length scales causing variability in the vertical velocity and temperature time series during each period.

Figure 6 shows the vertical profiles of potential temperature, wind speed and Brunt-Väisälä frequency, $N = [(g/\theta)(\partial\theta/\partial z)]^{1/2}$ observed within the lowest 300 m during the approximate times that the spectra were computed. Inspection of Figure 6 indicates a significant strengthening of the wind shear and deepening of the ABL between the two measurement periods. During both periods, large values of N are observed immediately above the ABL, with smaller values both within the ABL and above the lower portion of the overlying temperature inversion.

The spectra computed during the beginning of January 15 indicate energy at both small and large length scales, with a clearly discernible spectral gap at intermediate frequencies. Variability associated with the largest expected eddy, with a length scale equal to the ABL height, approximately 60 m, would yield a frequency of approximately 0.07 Hz advecting across the sensor at the mean wind speed of 4.1 m s^{-1} at the sensor height. Therefore power at

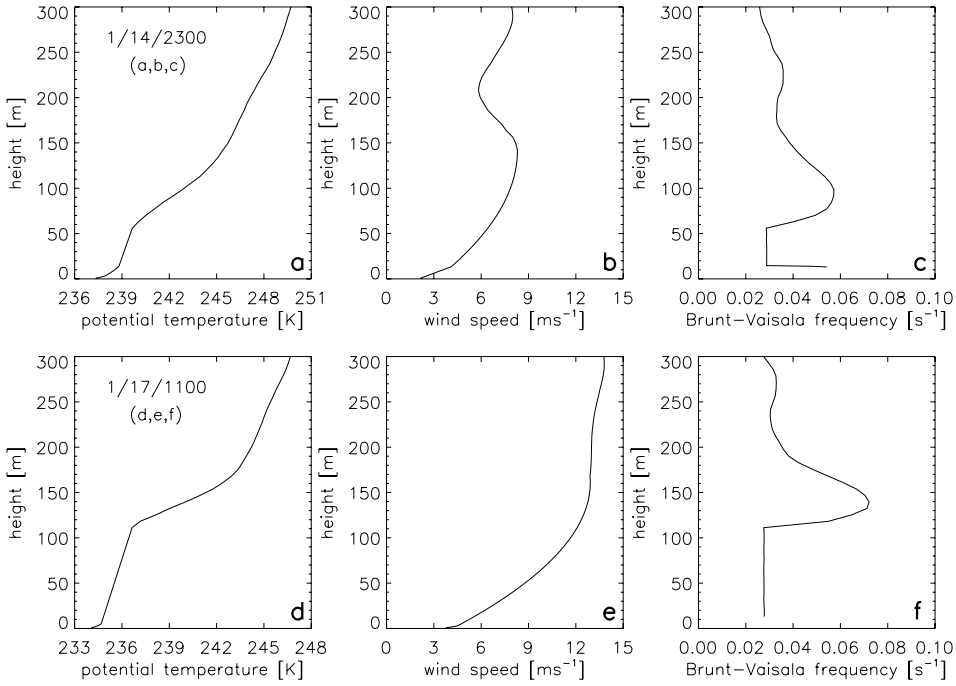

Figure 6. Profiles of potential temperature (panels a, d), wind speed (panels b, e) and Brunt–Väisälä frequency (panels c, f) nearest to the mid-January spectra computations.

higher frequencies indicates the presence of smaller-scale turbulent eddies. The power at frequencies lower than those within the spectral gap indicates wave activity on time scales of a few to tens of minutes. Some of the low-frequency power could indicate intermittent Kelvin–Helmholtz instability as well.

The spectra computed during January 17 differ quite markedly from those discussed above. One key difference is that the spectral power at high frequencies is an order of magnitude greater, indicating increased small-scale variability and stronger turbulent mixing. The second key difference is that although the power at low frequencies represents a much smaller proportion of the total variability, it is of similar magnitude to the earlier case, indicating that the same processes with large length scales were still occurring. The third key difference is that the range of frequencies where a spectral gap was previously observed now contains much more power. The increased power occurring within the intermediate wavelengths between those associated with wave activity and turbulence suggests the possibility of wave-turbulence interaction. The increased wind shear could also have enhanced Kelvin–Helmholtz instability.

5.2. Clear spring period

Two aircraft flights measuring high-frequency temperature and wind velocity data were conducted during the clear period in late May. One flight took place approximately 27 h prior to the beginning of clear period 4, the other occurred at approximately hour 46 of that period. High-frequency temperature and wind speed data near the surface were also recorded at the ASFG site during this period.

Panels a and c in Figure 7 show the vertical velocity spectra from a height of approximately 11 m on the ASFG tower during the 12-h periods preceding and following each of the turbulence measurement flights. Panels b and d show the corresponding temperature spectra. The spectra from the five hours identified in the legend show the intensities and the ranges of physical length scales causing the variability in vertical velocity and temperature time series during each period, and how they vary with the diurnal cycle during the spring.

Profiles of temperature, wind speed and Brunt-Väisälä frequency during flights 6 and 7 are shown in Figure 8. The key difference between the two periods is the magnitude of the wind shear occurring within the lowest approximately 300 m of the atmosphere. During flight 6, winds were relatively weak. A mixed layer driven by surface heating occupied the lowest approximately 100 m, above which a strong temperature inversion was observed. In contrast, during flight 7 the winds were considerably stronger with much greater vertical shear in the lowest 300 m. The potential temperature profile featured a weakly stable layer extending approximately 100 m above the surface, capped again by a strong inversion. While the profile of N during flight 7 resembles those from the winter periods, with large values immediately above the ABL, bounded by smaller values both above and below, the weaker and more uniform stability above the ABL during flight 6 is reflected by smaller, more uniform values of N above the ABL.

The spectra from 1300 UTC 20 May to 1300 UTC 21 May, shown in panels a and b of Figure 7, indicate significant temporal variability over the diurnal cycle. The weak winds occurring during this period allowed the surface temperature to decouple from that of the lower atmosphere, allowing for a significant diurnal oscillation of the sensible heat flux at the surface, from positive to negative values. During the late afternoon (0000 UTC), the surface temperature warmed above that of the atmosphere, inducing a positive surface heat flux and strong turbulent mixing in the lowest approximately 100 m. Late at night (1300 UTC), the surface temperature cooled below that of the atmosphere, resulting in stabilization of the ABL. Each of the late night periods featured a weak acceleration of the winds aloft. Wind speed peaked at 7.5 m s^{-1} at 90 m during 1300 UTC 20 May, fell to a peak of 3.5 m s^{-1} at 150 m during 0000 UTC 21 May, then rose again to a peak of

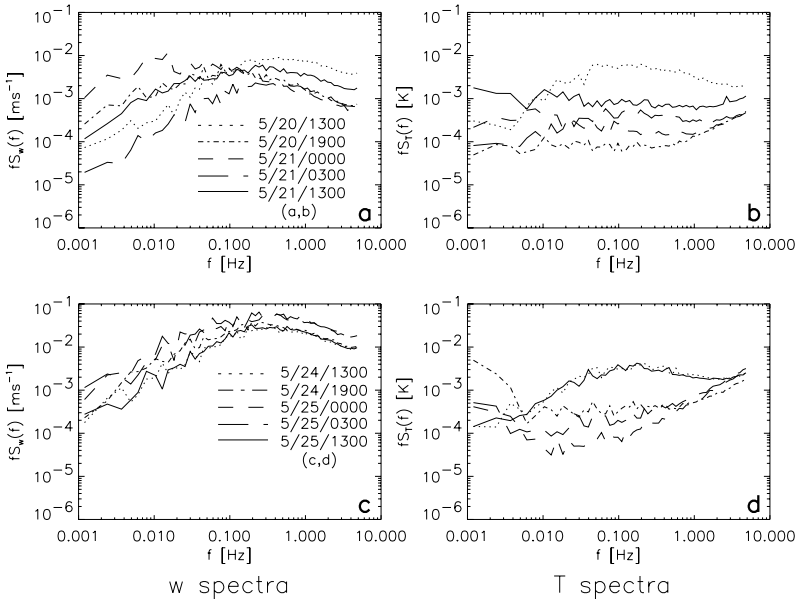

Figure 7. Vertical velocity spectra (panels a, c) and temperature spectra (panels b, d) obtained from the ASFG tower during late-May.

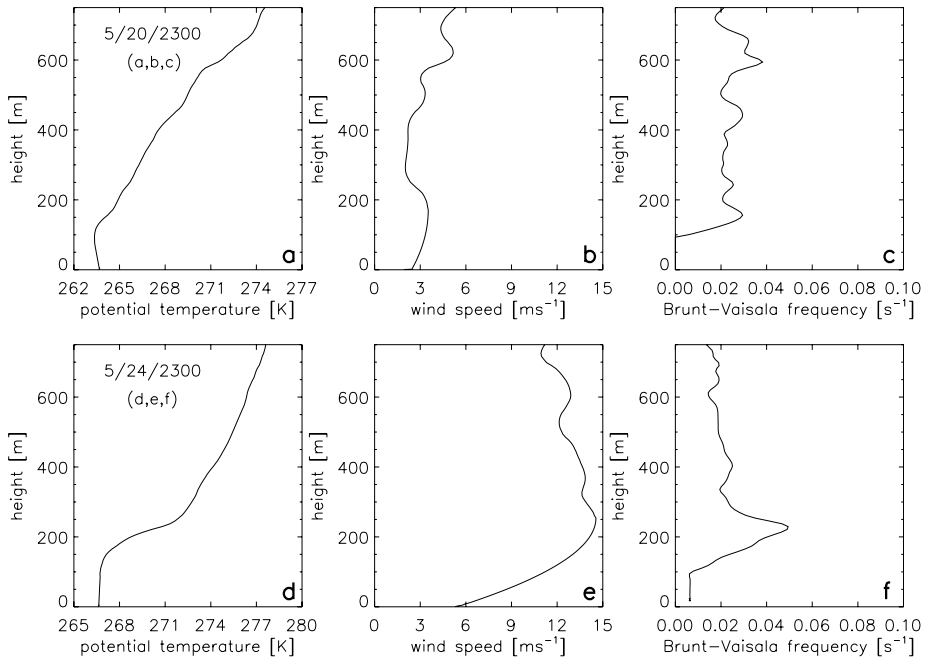

Figure 8. Profiles of potential temperature (panels a, d), wind speed (panels b, e) and Brunt–Väisälä frequency (panels c, f) nearest to flights 6 and 7.

5.3 m s^{-1} at 100 m about 1300 UTC 21 May. The spectra show the highest variability at small length scales during the late night hours, during the times of greatest vertical wind shear.

During the afternoon (1900-0000 UTC), the spectral energies at low frequencies increased significantly, while variability at higher frequencies diminished. One explanation of this diurnal variability of the vertical velocity spectra is the generation of waves resulting from the impingement of turbulent eddies upon the base of the temperature inversion. After the peak of the solar cycle (0300 UTC), spectral energies decreased across all frequencies, as the impulses triggering gravity wave activity diminished, and vertical wind shear remained weak. By 1300 UTC vertical wind shear had increased, and spectral energies had returned to levels similar to those observed 24 h previously. The temperature spectra show the highest energies during the late night hours, when the temperature profiles were the most stable. During the afternoon hours, mixing destabilized the temperature profile such that vertical excursions caused less variability in the temperature time series.

The temperature spectra computed during the 24-h period surrounding flight 7, shown in panels c and d of Figure 7, are quite similar to those of flight 6, with the peak variability likewise occurring during the most stable portion of the diurnal cycle. However the vertical velocity spectra are very different. During flight 7, the winds were much stronger, causing much more vigorous mixing throughout the lower atmosphere, reflecting the increase in power across most of the spectra. Additionally the diurnal variability in spectral power was smaller during the latter period, as the sustained winds maintained mixing overnight. During the period surrounding flight 7, the fluxes of heat into the surface were a sink for turbulence kinetic energy within the ABL. During the overnight hours, the increased removal of heat from the ABL reduced the energy across the entire spectrum slightly, implying some connection between the wave and turbulence fields. During the afternoon, solar warming of the surface mitigated the flow of energy into the surface, allowing the achievement of greater energy across the spectra.

As Figure 8 shows, the more vigorous mixing did not completely destabilize the temperature profile within the ABL as during flight 6. This discrepancy may be explained by two processes, an increased flux of energy into the surface, cooling the ABL from below, and the entrainment of warmer air from above the ABL, warming it from above.

Figure 9 depicts vertical velocity spectra and vertical velocity and potential temperature cospectra calculated from data collected during flight 6. For each of the spectra shown in Figure 9, a frequency of 1 Hz corresponds to a wavelength of approximately 100 m, as the aircraft was moving at approximately 100 m s^{-1}. The mean height of each leg of the flight as well as the local gradient Richardson number Ri computed from Equation (6) using the

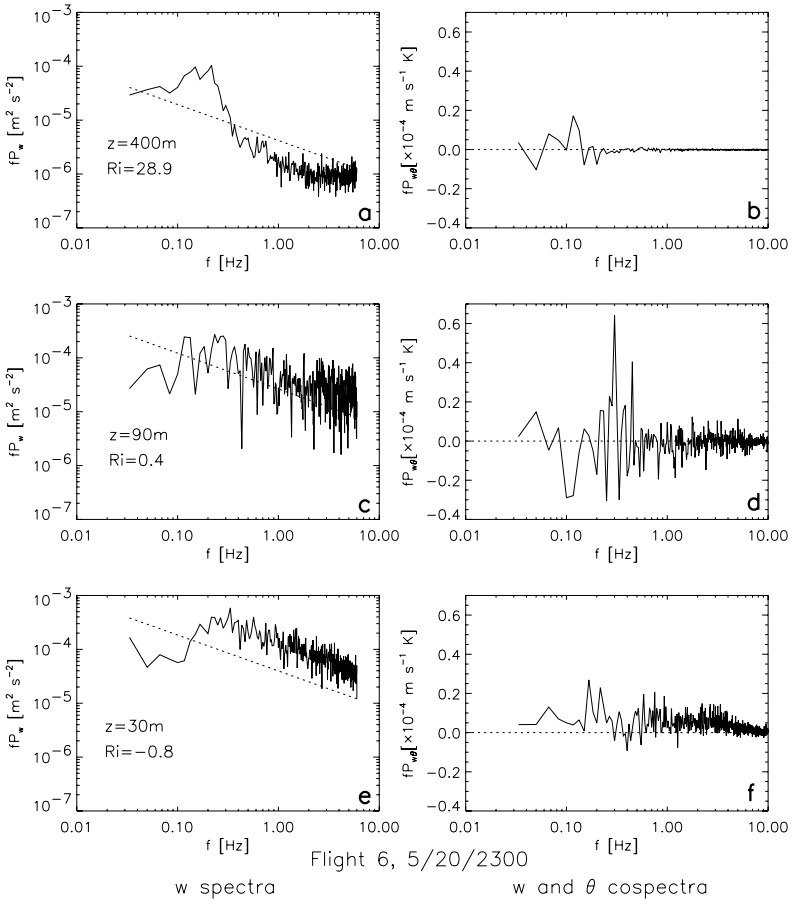

Figure 9. Vertical velocity spectra (panels a, c, e) and vertical velocity and potential temperature cospectra (panels b, d, f) from three legs during flight 6. Dotted lines in spectra indicate −2/3 slope of the inertial subrange. Dotted lines in cospectra indicate zero.

radiosonde temperature, pressure and wind speed profiles, are indicated in each panel.

During flight 6, the lowest two legs took place in the shallow ABL beneath the temperature inversion. The value of $Ri = -0.8$ at 30 m indicates a superadiabatic layer near the surface. A flux of sensible heat flux from the surface into the atmosphere during flight 6 drove strong turbulent mixing in the lower portion of the ABL. At 90 m, the value of $Ri = 0.4$ was slightly higher than the critical value of $Ri = 0.2$–0.3, where the theoretical threshold for turbulence lies, indicating that the upper portion of the ABL was not as well mixed as the lower portion, but still much more mixed than the inversion above. At 400 m, the value of $Ri = 28.9$ indicates the very strong stability within the temperature inversion.

The spectra and cospectra at 30 and 90 m reflect the strong mixing at small length scales within the ABL associated with turbulence. The power at small wavelengths at 400 m is approximately two orders of magnitude lower than the high-frequency power within the ABL, reflecting very little turbulence within the stable inversion. The spectra and cospectra at all heights indicate considerable low-frequency power, all manifesting maximum power at wavelengths larger than the largest expected turbulent eddy and well within the range of length scales associated with gravity waves. During flight 6, eddies the size of the ABL, ~ 100 m, would cause variability at a frequency of approximately 0.83 Hz, given the aircraft velocity of approximately 100 m s^{-1}.

The spectral peak at 400 m at frequencies of 0.1–0.2 Hz indicates gravity waves with lengthscales in the range of 500–1000 m. The spectra at 30 and 90 m show a similar low-frequency spectral peak, however at these heights power is distributed over a wide range of smaller length scales. This energy in a region of the spectrum between the gravity waves observed at 400 m and the largest expected turbulent eddies indicates possible wave turbulence interaction, such as the breaking of gravity waves generated aloft as they interact with smallscale turbulence within the ABL.

Figure 10 depicts the same information as Figure 9 collected during flight 7. During flight 7 only one leg was flown within the ABL, at 90 m, and two legs were flown at a height of 700 m, which was about 550 m above the top of the ABL. The value of $Ri = -0.05$ at 90 m indicates instability and strong mixing within the ABL during flight 7. Although the value of $Ri = 0.35$ at 700 m is only slightly supercritical, the spectra and cospectra computed at 700 m indicate very little power, especially at high frequencies.

The spectra and cospectra at 90 m indicate significant energy occurring at wavelengths up to 1000 m, which is approximately a factor of 5 larger than the largest expected turbulent eddy. During flight 7, eddies the size of the ABL, 150 m would cause variability at approximately 0.67 Hz. The energy at wavelengths in the vicinity of this characteristic length scale once again suggests possible interactions between the wave and turbulence fields.

Figure 11 shows vertical velocity variances ($\overline{w'w'}$) and vertical heat fluxes ($\overline{w'\theta'}$) computed by integrating over the spectra and cospectra discussed above. The four symbols plotted at each height are their computed values obtained by integrating from four different low-frequency endpoints, or cutoff wavelengths.

During flight 6, as the 30 and 90 m legs were each within the ABL, the vertical velocity variance shows positive values at each of those heights. The positive heat flux values at 30 m reflect the superadiabatic potential temperature profile within the lower portion of the ABL. During the hour of flight 6, the ASFG site measured a sensible heat flux at the surface of 6.5 W m^{-2}, indicating the upward flow of heat from the surface. The small

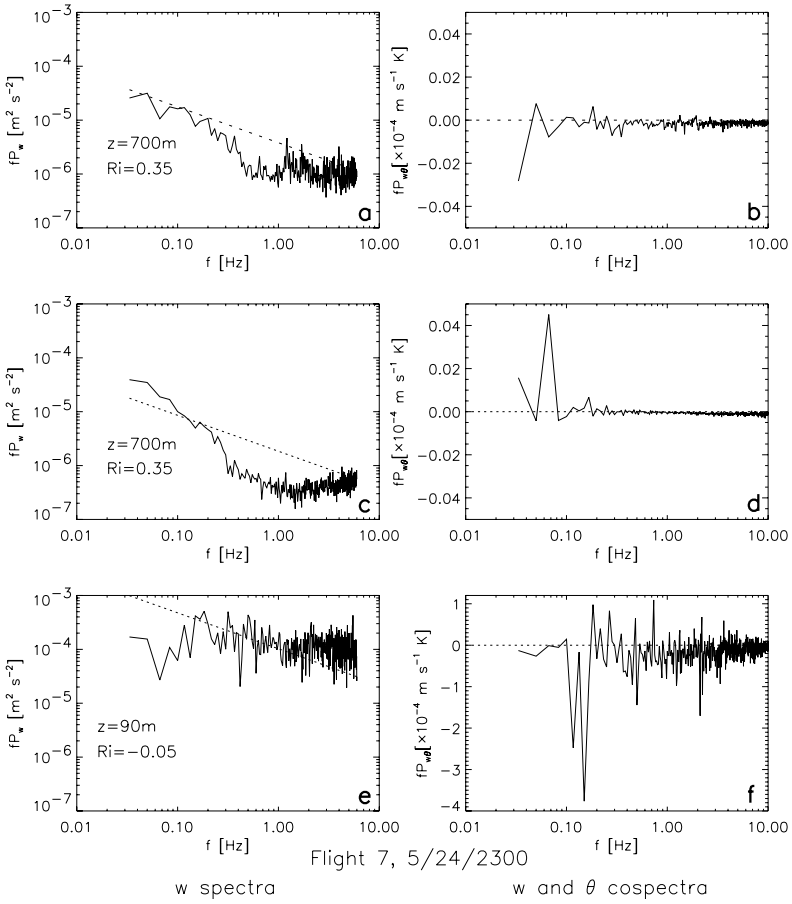

Figure 10. Vertical velocity spectra (panels a, c, e) and vertical velocity and potential temperature cospectra (panels b, d, f) for three legs during flight 7. Dotted lines in spectra indicate $-2/3$ slope of the inertial subrange. Dotted lines in cospectra indicate zero.

and variable heat flux values at 90 m indicate the neutrally stratified environment of the upper ABL, where mixing was weaker, and entrainment of the warmer air from above may have been counterbalancing the upward flux of heat from below. The variance and flux are nearly zero at 400 m due to the weak turbulence far above the ABL top.

During flight 7, the vertical velocity variance at 90 m was similar to that observed at 30 m during flight 6, however the vertical heat flux in the upper ABL during flight 7 was downward and much larger. The sign of the heat flux at 90 m is consistent with the downward surface heat fluxes measured during the period surrounding flight 7, as seen in Figure 3. The $-0.3\,\mathrm{W\,m^{-2}}$ surface heat flux value measured during the hour of the 90 m leg of flight 7 was the smallest measured that afternoon, with much larger (downward) values

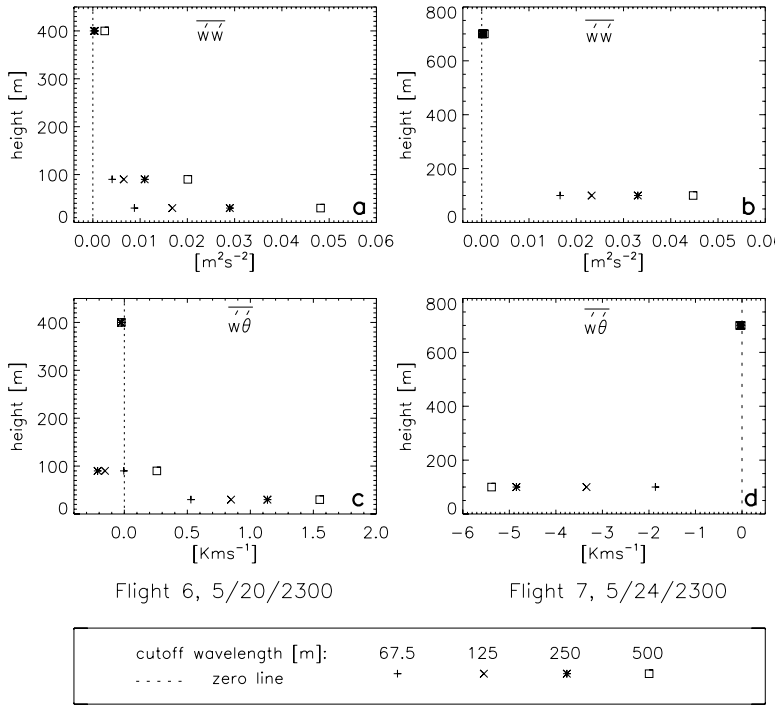

Figure 11. Vertical fluxes of momentum (panels a, c) and heat (panels b, d) computed from data taken during flights 6 and 7 using various cut-off wavelengths.

during the preceding hours. These large sustained downward fluxes, coupled with the large heat flux measured near the ABL top during flight 7 suggest a significant entrainment of heat into the ABL and downward flux of heat through the ABL and into the surface during the period. As with flight 6, the variance and heat flux are nearly zero far above the ABL top, where turbulence was very weak.

Although the atmosphere during flight 7 would be characterized as more 'stable' than during flight 6, the magnitudes of the calculated fluxes using the various cut-off wavelengths are larger by factors of approximately 3–4 during flight 7. Hence, there is much more energy flowing vertically within the more 'stable' atmosphere occurring during flight 7 than within the 'unstable' atmosphere occurring during flight 6.

The relationship between the cut-off wavelengths used in the computations of the variances and fluxes suggests that wave activity and wave-turbulence interactions were important components of the energetics and heat exchange processes occurring within the ABL during each of these flights. The increase in the magnitudes of the computed variances and heat fluxes as the low-frequency starting point for the spectral integration is moved to larger and larger wavelengths indicates that processes with length scales larger than the

largest hypothetical turbulent eddies were interacting with the turbulence field, thereby contributing significantly to the vertical exchange of heat.

6. Summary and Conclusions

Although skies are typically cloudy in the Arctic, many extended clear-sky periods occur throughout the annual cycle, particularly during the winter. As clouds are a significant source of radiative heating for the surface, their absence during clear-sky periods has a profound effect on the energy balance at the surface of the snow/ice pack. In the absence of cloud radiative forcing, the flow of sensible heat within the lower atmosphere and its turbulent transport to and exchange with the surface comprise significant components of both the surface and lower atmospheric heat budgets during such periods.

Time-averaged surface heat budgets were estimated for several periods of the SHEBA experiment during which either predominantly clear or cloudy conditions prevailed. During the cloudy periods, weak radiative cooling at the surface was nearly balanced by conductive heat fluxes of similar magnitudes, with generally small net turbulent fluxes of heat. During the clear periods occurring in the winter, much stronger surface cooling was balanced by much larger conductive heat fluxes and significant turbulent heat fluxes as well. Surface heat budget calculations performed during one cloudy and one clear-sky period in the spring yielded similar changes in the relationships between the various surface fluxes between cloudy and clear-sky conditions, although the presence of the solar cycle resulted in a much smaller radiative cooling during the clear period, and a net radiative warming of the surface during the cloudy period.

Analysis of the lower-atmospheric heat budget during a representative nearly steady 72-h clear-sky period suggests that, to first order, the heat extracted from the ABL by sensible heat fluxes at the surface was balanced by the entrainment of heat into the ABL from above. A significant portion of the warming occurring above the ABL to balance the loss of heat due to entrainment was accomplished by the interaction of subsiding motions with the strong temperature gradient occurring there. Turbulence generated by a combination of low-level wind shear and wave activity provided the mechanism for the entrainment of this heat into the ABL, and for its diffusion down to and exchange with the surface. Extension of these results to the longer-term, predominantly clear-sky, periods occurring during the low-sun seasons is supported by the thermodynamic structure and evolution of the lower atmosphere relative to the large-scale synoptic conditions during those periods.

The importance of this lower atmospheric heat exchange process to the ice pack mass budget is potentially significant as well. Turbulent heat fluxes at the surface, in combination with the other energy exchange processes occurring there, play an important role in determining the surface temperature, internal snow/ice temperatures, and ultimately influence the growth/ablation of snow and ice.

The above outlined scenario for heat transfer presents a challenge to modelling due to the small spatial scales of the relevant phenomena, and the weak and intermittent nature of the mixing regime. Extremely high vertical resolutions are required to fully resolve the strong temperature gradients existing within the lower atmosphere during such periods, and to obtain the correct heating rates due to the interaction of these strong gradients with subsidence. Extremely high resolutions in both the vertical and horizontal directions are likewise required to resolve the Kelvin–Helmholtz and gravity wave activity occurring throughout such periods, as well as the interactions between the wave and turbulence fields. That being the case, the investigation of subgrid-scale parameterizations for these processes is the preferred course of action. Despite such difficulties, these small-scale processes are important components of the vertical energy exchanges occurring within the lower atmosphere and between the atmosphere and the surface of the Arctic Ocean ice pack during stable, clear-sky periods, and their effects should be incorporated into studies thereof.

Acknowledgements

The authors extend their gratitude to the many people who lent assistance to this effort, especially Ola Persson, who provided the ASFG data and made many helpful suggestions which improved the manuscript, Andrey Grachev, who provided the spectra from the ASFG tower, James Pinto and Hugh Morrison. Also we thank two anonymous reviewers for their helpful comments, which greatly improved the manuscript. Additionally we thank our colleagues in the SHEBA Atmospheric Surface Flux Group, Ed Andreas, Chris Fairall, Peter Guest, and Ola Persson for help collecting and processing the data. The National Science Foundation supported this research with grants to the U.S. Army Cold Regions Research and Engineering Laboratory, NOAA's Environmental Technology Laboratory, and the Naval Postgraduate School. This work was performed under the auspices of the U.S. Department of Energy at the University of California, Lawrence Livermore National Laboratory under Contract W-7405-Eng-48. The research was also funded by a grant from the National Science Foundation Arctic Systems Science Program.

References

Andrén, A.: 1995, 'The Structure of Stably Stratified Atmospheric Boundary Layers: A Large-Eddy Simulation Study', *Quart. J. Roy. Meteorol. Soc.* **121**, 961–985.

Cheung, T. K.: 1991, 'Sodar Observations of the Stable Lower Atmospheric Boundary Layer at Barrow, Alaska', *Boundary-Layer Meteorol.* **57**, 251–274.

Chimonas, G.: 1980, 'Waves, Stability and Turbulence', in J. C. Wyngaard (ed.) *Workshop on the Planetary Boundary Layer*, Amer. Meteor. Soc., Boston, Massachusetts, 392 pp.

Curry, J. A. and Ebert, E. E.: 1992, 'Annual Cycle of Radiative Fluxes over the Arctic Ocean' *J. Climate* **5**, 1267–1280.

Curry, J. A., Rossow, W. B., Randall, D., and Schramm, J. L.: 1996, 'Overview of Arctic Cloud and Radiation Characteristics', *J. Climate* **9**, 1731–1764.

Derbyshire, S. H.: 1990, 'Nieuwstadt's Stable Boundary Layer Revisited', *Quart. J. Roy. Meteorol. Soc.* **116**, 127–158.

Fairall, C. W., Bradley, E. F., Rogers, D. P., Edson, J. B., and Young, G. S.: 1996, 'Bulk Parameterization of Air-Sea Fluxes for Tropical Ocean-Global Atmosphere Coupled-Ocean Atmosphere Response Experiment', *J. Geophys. Res.* **101**, 3747–3764.

Forrer, J. and Rotach, M. W.: 1997, 'On the Turbulence Structure in the Stable Boundary Layer over the Greenland Ice Sheet ', *Boundary-Layer Meteorol.* **85**, 111–136.

Finnigan, J. J.: 1988, 'Kinetic Energy Transfer Between Internal Gravity Waves and Turbulence', *J. Atmos. Sci.* **45**, 486–505.

Finnigan, J. J. and Einaudi, F.: 1981, 'The Interaction Between an Internal Gravity Wave and the Planetary Boundary Layer. Part II: The Effect of the Wave on the Turbulence Structure', *Quart. J. Roy. Meteorol. Soc.* **107**, 807–832.

Fua, P., Chimonas, G., Einaudi, F., and Zeman, O.: 1982, 'An Analysis of a Wave Turbulence Interaction', *J. Atmos. Sci.* **39**, 2450–2463.

Hahn, C. J., Warren, S. G., London, J., Chervin, R. M., and Jenne, R. L.: 1984, 'Atlas of Simultaneous Occurrence of Different Cloud Types Over Land', NCAR Tech. Note, TN-241 + STR, 21 pp.

Handorf, D., Foken, T., and Kottmeier, C.: 2000, 'The Stable Atmospheric Boundary Layer over an Antarctic Ice Sheet', *Boundary-Layer Meteorol.* **91**, 165–189.

Hooke, W. H., Hall, F. F., and Gossard, E. E.: 1973, 'Observed Generation of an Atmospheric Gravity Wave by Shear Instability in the Mean Flow of the Planetary Boundary-Layer', *Boundary-Layer Meteorol.* **5**, 29–41.

Huschke, R. E.: 1969, 'Arctic Cloud Statistics From Air-Calibrated Surface Weather Observations', The Rand Corporation, RM-6173-PR, 79 pp.

Intrieri, J. M., Shupe, M. D., Uttal, T., and McCarty, B. J.: 2002a, 'Annual Cycle of Arctic Cloud Geometry and Phase from Radar and Lidar at SHEBA', *J. Geophys. Res.* **107**(C10), 8030, doi:10.1029/2000JC000432.

Intrieri, J. M., et al.,: 2002b, 'An Annual Cycle of Arctic Surface Cloud Forcing at SHEBA', *J. Geophys. Res.* **107**(C10), 8039, doi:10.1029/2000JC000439.

IPCC: 2001, *Climate Change 2001, The Scientific Basis*, Cambridge University Press, New York, 881 pp.

Kondo, J., Kanechika, O., and Yosuda, N.: 1978, 'Heat and Momentum Transfers under Strong Stability in the Atmospheric Surface Layer', *J. Atmos. Sci.* **35**, 1012–1021.

Kim, J. and Mahrt, L.: 1992, 'Simple Formulation of Turbulent Mixing in the Stable Free Atmosphere and Nocturnal Boundary layer', *Tellus* **44A**, 381–394.

Kosović, B. and Curry, J. A.: 2000, 'A Large Eddy Simulation of a Quasi-Steady, Stably Stratified Atmospheric Boundary Layer', *J. Atmos. Sci.* **57**, 1052–1068.

Larsen, S. E., Courtney, M., and Mahrt, L.: 1990, 'Low Frequency Behavior of Horizontal Power Spectra in Stable Surface Layers', in Proceedings of the 9th AMS Symposium on Turbulence and Diffusion, pp. 401–404.

Mahrt, L.: 1999, 'Stratified Atmospheric Boundary Layers', *Boundary-Layer Meteorol.* **90**, 375–396.

Mahrt, L. and Vickers, D.: 2001, 'Contrasting Vertical Structures of Nocturnal Boundary Layers', *Boundary-Layer Meteorol.* **105**, 351–363.

Mason, P. J. and Derbyshire, D. J.: 1990, 'Large-Eddy Simulation of the Stably Stratified Atmospheric boundary Layer', *Boundary-Layer Meteorol.* **53**, 117–162.

Maykut, G. A.: 1982, 'Large-Scale Heat Exchange and Ice Production in the Central Arctic', *J. Geophys. Res.* **87**, 7971–7984.

Mlawer, E. J., Taubman, S. J., Brown, P. D., Iacono, M. J., and Clough, S. A.: 1997, 'Radiative Transfer for Inhomogeneous Atmospheres: RRTM a Validated Correlated-k Model for the Longwave', *J. Geophys. Res.* **102**, 16663–16682.

Nappo, C. J.: 1990, 'Sporadic Breakdowns of Stability in the PBL Over Simple and Complex Terrain', *Boundary-Layer Meteorol.* **54**, 69–87.

Nappo, C. J.: 2002, *An Introduction to Atmospheric Gravity Waves*, Academic Press, 276 pp.

Persson, P. O. G., Fairall, C. W., Andreas, E. L., Guest, P. S., and Perovich, D. K.: 2002, 'Measurements near the Atmospheric Surface Flux Group Tower at SHEBA: Site Description, Data Processing, and Accuracy Estimates', NOAA Tech. Memo. OAR ETL (available at the National Technical Information Service, 5285 Port Royal Road, Springfield, VA 22061).

Przybylak, R.: 2003, *The Climate of the Arctic*, Kluwer Academic Publishers, Dordrecht, 270 pp.

Saiki, E. M., Moeng, C., and Sullivan, P.S.: 2000, 'Large-Eddy Simulation of the Stably Stratified Planetary Boundary Layer', *Boundary-Layer Meteorol.* **95**, 1–30.

Sempreviva, A., Larsen, E., and Mortensen, N. G.: 1992, 'Experimental Study of Flow Modification Inland from a Coast for Non-Neutral Conditions', RISØ M–2924.

Schweiger, A. J. and Key, R. J.: 1994, 'Arctic Ocean Radiative Fluxes and Cloud Forcing Estimates from the ISCCP C2 Cloud Dataset, 1983–1990', *J. Appl. Meteorol.* **33**, 948–963.

Smedman, A. S.: 1988, 'Observations of a Multi-level Turbulence Structure in a Very Stable Atmospheric Boundary Layer', *Boundary-Layer Meteorol.* **44**, 231–253.

Stull, R. B.: 1988, *An Introduction to Boundary Layer Meteorology*, Kluwer Academic Publishers, Dordrecht, 666 pp.

Sturm, M., Holmgren, J., and Perovich, D. K.: 2001, 'Spatial Variability in the Winter Heat Flux at SHEBA: Estimates from Snow-Ice Interface temperatures', *Annals of Glaciol* **33**, 213–220.

Sturm, M., Perovich, D. K., and Holmgren, J.: 2004, 'Thermal Conductivity and Heat Transfer Through the Snow on the Ice of the Beaufort Sea', *J. Geophys. Res.* **107**, 10.1029/2000JC000409.

Uttal, T., et al.: 2002, 'The Surface Heat Budget of the Arctic Ocean', *Bull. Am. Meteorol. Soc.* **83**, 255–275.

Walsh, J. E. and Chapman, W. L.: 1998, 'Arctic Cloud-Radiation-Temperature Associations in Observational Data and Atmospheric Reanalysis', *J. Climate* **11**, 3030–3044.

Warren, S. G., Hahn, C. J., London, J., Chervin R. M., and Jenne, R. L.: 1988, 'Global Distribution of Total Cloud Cover and Cloud Type Amounts Over the Arctic Ocean', NCAR Tech. Note, TN-317 + STR, 212 pp.

Zhang, T., Stamnes, K., and Bowling, S. A.: 1996, 'Impact of Clouds on Surface Radiation Fluxes and Snowmelt in the Arctic and Subarctic', *J. Climate* **9**, 2110–2123.

Zilitinkevich, S. S. and Mironov, D. V.: 1996, 'A Multi-Limit Formula for the Equilibrium Depth of a Stably Stratified Boundary Layer', *Boundary-Layer Meteorol.* **81**, 325–351.